SANDIA REPORT
SAND20XX-XXXX
Printed Click to enter a date

Sandia National Laboratories

Strength of porous α-SiO_2 in a shock loaded environment

Matthew Hudspeth[1], Joe Olles[2], James Williams[2], Anirban Mandal[1], Seth Root[2], Tracy Vogler[3]
[1]Los Alamos National Laboratory, Los Alamos, NM, 87543
[2]Sandia National Laboratories, Albuquerque, NM, 87905
[3]Sandia National Laboratories, Livermore, CA, 94550

Prepared by
Sandia National Laboratories
Albuquerque, New Mexico
87185 and Livermore,
California 94550

Issued by Sandia National Laboratories, operated for the United States Department of Energy by National Technology & Engineering Solutions of Sandia, LLC.

Available to DOE and DOE contractors from
U.S. Department of Energy
Office of Scientific and Technical Information
P.O. Box 62
Oak Ridge, TN 37831

Telephone:	(865) 576-8401
Facsimile:	(865) 576-5728
E-Mail:	reports@osti.gov
Online ordering:	http://www.osti.gov/scitech

Available to the public from
U.S. Department of Commerce
National Technical Information Service
5301 Shawnee Rd
Alexandria, VA 22312

Telephone:	(800) 553-6847
Facsimile:	(703) 605-6900
E-Mail:	orders@ntis.gov
Online order:	https://classic.ntis.gov/help/order-methods/

ABSTRACT

The strength of brittle porous media is of concern in numerous applications, for example, earth penetration, crater formation, and blast loading; thus it is of importance to possess techniques that allow for constitutive model calibration within the laboratory setting. It is the goal of the immediate work to demonstrate an experimental technique allowing for strength assessment, which can be implemented into pressure dependent yield surfaces within numerical simulation schemes. As a case study, the deviatoric strength of distended α-SiO_2 has been captured in a tamped Richtmyer-Meshkov instability environment at a pressure regime of 4-10 GPa. In contrast to traditional RMI studies used to infer strength in solids, the described approach herein is implemented to probe the behavior of the porous tamp media backing the corrugated solid surface. Hydrocode simulation has been used to interpret the experiment, and a resulting pressure-dependent yield surface akin to the often employed Modified Drucker-Prager model has been calibrated via the coupled experiment and simulation. The simulations indicate that the resulting jet length generated by the RMI is highly sensitive to the porous media strength, thereby providing a feasible experimental platform capable of capturing pressurized granular deviatoric response. Additionally, a Mach lens loading environment has also been implemented as a validation case study, demonstrating good agreement between experiment and simulation within an alternative loading environment. Calibration and validation of the pressure-dependent yield surface gives confidence to the model form, thereby providing a framework for future porous media strength studies.

ACKNOWLEDGEMENTS

We thank the staff at the Dynamic Compression Sector within the Advanced Photon Source at Argonne National Laboratory for their tireless efforts at commissioning, and now executing operations at a demanding user facility. Without their efforts, none of this work would have been possible. The first author would also like to thank the LDRD office of Sandia National Laboratories for funding this work.

CONTENTS

LIST OF FIGURES

LIST OF TABLES

This page left blank

ACRONYMS AND DEFINITIONS

Abbreviation	Definition
RMI	Richtmyer-Meshkov Instability
EOS	Equation of State
DCS	Dynamic Compression Sector
APS	Advanced Photon Source
ANL	Argonne National Laboratory
SEM	Scanning Electron Microscope
PCI	Phase Contrast Imaging
EPP	Elastic-Perfectly Plastic

1. INTRODUCTION

The dynamic high-pressure strength of porous brittle solids is of interest in a number of earth engineering and science applications, for example, mining, earth penetration, and crater formation. Depending on the subjected drive pressure and geometry of the dynamic event, the yield behavior of the porous media can be essential in understanding the resulting state variables and wave evolution in such environments. Within the soil compression community, a variety of yield surfaces are often employed (e.g. Drucker-Prager, Von-Mises, Prantl-Reuss [1, 2]), and are commonly calibrated to exhibit yield behavior following available strength data in literature; most often such data is limited to confined quasi-static testing or elevated strain-rate experiments performed on a triaxial split-Hopkinson bar apparatus. Therefore, although such a calibration approach is indeed appropriate when modelling a dynamic event undergoing similar strain-rates and pressures regimes to the employed calibration, it may be somewhat in error when studying impact events exhibiting strain-rates and/or pressures greater in magnitude by several orders. As such, it is desirable to possess an experimental technique probing a relevant pressure/strain-rate regime that can directly measure the resulting yield behavior, or can assess the constitutive response through numerical analysis with minimal tuning parameter functions.

In efforts to study the strength behavior of porous media up to pressures of 3 GPa, LaJuenesse et al. [3] and Vogler et al. [4] have utilized the traditional pressure-shear technique [5] generally used to study strength in solids in low shock-pressure environments. Additionally, LaJuenesse predicted an extension of the yield surface to pressures nearing 5 GPa via mesoscale modelling within a hydrocode environment, due to experimental issues of anvil elasticity limits and slip conditions at the sample-anvil interfaces [3]. To further drive to higher pressure regimes via experiment, Vogler applied a novel perturbation decay technique to WC powders [6]. The approach, with rich history in high-pressure fluid viscosity measurements [7, 8], calibrates the yield criterion with numerical hydrocode analysis, via tracking the progression of a sinusoidal compaction front driven into the granular target. Implementing a geologic pressure-dependent yield surface similar to a Prandtl-Reuss criterion [9, 10], Vogler found sufficient sensitivity in the strength calibration at a shock pressure of 5.5 GPa in the sample [6], resulting in a yield strength at said pressure of roughly 1 GPa.

Interestingly, the geometry used by Vogler [6] is nearly identical to an untamped Richtmyer-Meshkov instability (RMI) which is routinely employed by various researchers [11, 12, 13, 14, 15, 15, 16, 17] studying the strength of solids at elevated strain rates. In such a technique, an inversion of the corrugated back surface occurs, and a resultant jet is formed; the jet length is tracked via velocimetry and then used as a calibration for strength model tuning in numerical simulation at a specific strain-rate and temperature, off the released pressure state. Such an environment need not be limited to jet formation in vacuum, rather an amalgamation of early perturbation decay work [7, 8] and RMI jetting [11, 12, 13, 14, 15, 15, 16, 17] is indeed possible. Herein lies the heart of this work; the geometry introduced of a metal tamped with porous media is driven to a pressure state causing an RMI inversion, thereby allowing for calibration of the granular material yield surface. Section 2 will describe the RMI tamped environment with the powder material of interest, namely α-SiO_2. As the driver which is used to form jets must be well characterized, the calibration of the driver yield strength is discussed in the Appendix using a deuterium oxide (D_2O) tamp material behind the metallic driver. Finally in Section 3, the calibrated pressure-dependent yield surface of α-SiO_2 is interrogated in a validation experimental data set, wherein a Mach lens is driven into the α-SiO_2. The experimental Mach lens behavior is well captured in the numerical simulations using the calibrated α-SiO_2 yield surface from Section 2, thereby giving confidence in the calibrated constitutive model.

2. RICHTMEYER-MESHKOV INSTABILITY

2.1. Experimental

2.1.1. Material

In efforts to assess the strength of a brittle distended material, α-SiO_2 (Atlantic Equipment Engineers) powder was selected as a candidate for this non-planar compaction study. The as-received powder was dry-sieved to a particle size less than roughly 20 microns and had a nominal tap density of 1.55 g/cm^3. Morphology of the SiO_2 was highly faceted, which is demonstrated in Figure 2-1. OFHC copper was used as the driver material.

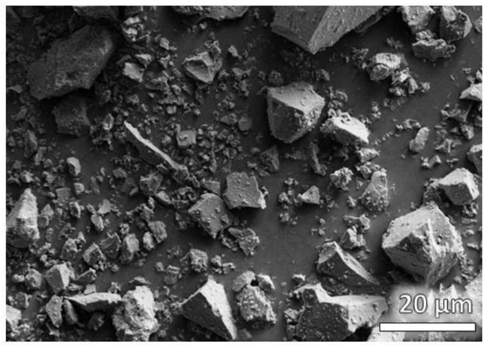

Figure 2-1. SEM of sample α-SiO_2 material

2.1.2. Experimental Setup

A schematic of the target assembly used in the granular tamped RMI experiment can be seen in Figure 2-2. A copper driver with a corrugated back-surface has been machined via climb-milling. As is common in untamped RMI experiments, a non-dimensional geometry of the target surface is defined by the "wavenumber" which is defined as $\eta_0 k$ in Equation 1,

$$\eta_0 k = \frac{2\pi}{\lambda}\eta_0 \qquad \text{(Eq. 2-1)}$$

wherein η_0 and λ represent the amplitude and wavelength of the profile, respectively. For the experiments described in this report, wavelengths were selected to be 1 mm, so as to allow for imaging of two perturbations in the radiography scheme. Wavenumbers were selected to be between one and two, depending on drive pressures, being designed *a priori* from estimates made in pre-shot scoping simulations. As will be described in Section 2.1.3, the ideal experiment generates an inversion of the wave profile to a jet that reaches a steady state length within the diagnostic field of view (~2 mm x 2 mm). Additionally, care must be taken to ensure that the wavenumber selection allows for inversion, but is not so great that the jet "mushrooms" as is common in classical fluid RMI experiments [18, 19].

A schematic of the capsule geometry can be seen in Figure 2-2. Sample assemblies were then loaded into the Dynamic Compression Sector (DCS) gun system located at the Advanced Photon Source (APS) as depicted in Figure 2-2 and impacted by either Cu or Ta flyers at velocities of ~1 – 2 km/s. The corrugated copper surface was tamped with α-SiO_2 powder, which was housed inside of a hollow cylindrical PMMA body having an inner diameter and height of 13.5 mm and 8.5 mm, respectively. The α-SiO_2 powder was packed to a nominal tap density of 1.55 g/cc. The X-ray beam was aligned perpendicular to the barrel-projectile axis and the sample assembly was rotated with a motorized rotation stage so as to look along the sinewave profiles.

A LSO:Ce (Lu_2SiO_5:Ce) scintillator with a decay time of roughly 40-80 μs was used to convert X-rays to visible light [20]. In efforts to increase brightness of the captured image, both sides of the scintillator were imaged; an objective lens was focused onto the downstream mirror, while the upstream objective lens was focused onto the X-ray transparent pellicle window. In this fashion, visible light generated by the scintillator is only halved once via beam splitters before arriving on the ICCD image plates. Coupled to the impact time of the flyer and target, the shock evolution in the housing/core was illuminated by a 23.1 keV pulse-separated X-ray beam generated from the U17 undulator placed within the storage ring of the APS. An ultra-fast 8-frame imaging system was implemented to capture the wave-profile history in the sample region of interest via phase contrast imaging (PCI), being temporally coupled to the X-ray bunch arrival at an inter-frame spacing of 153.4 ns. The resulting temporal resolution of the system was roughly 33.5 ps, being defined by the bunch length in the APS storage ring. The spatial resolution of the image is roughly defined by the pixel size in the ICCDs and the selected magnifier, for which in these experiments resulted in a pixel resolution of 2.59 μm/pixel.

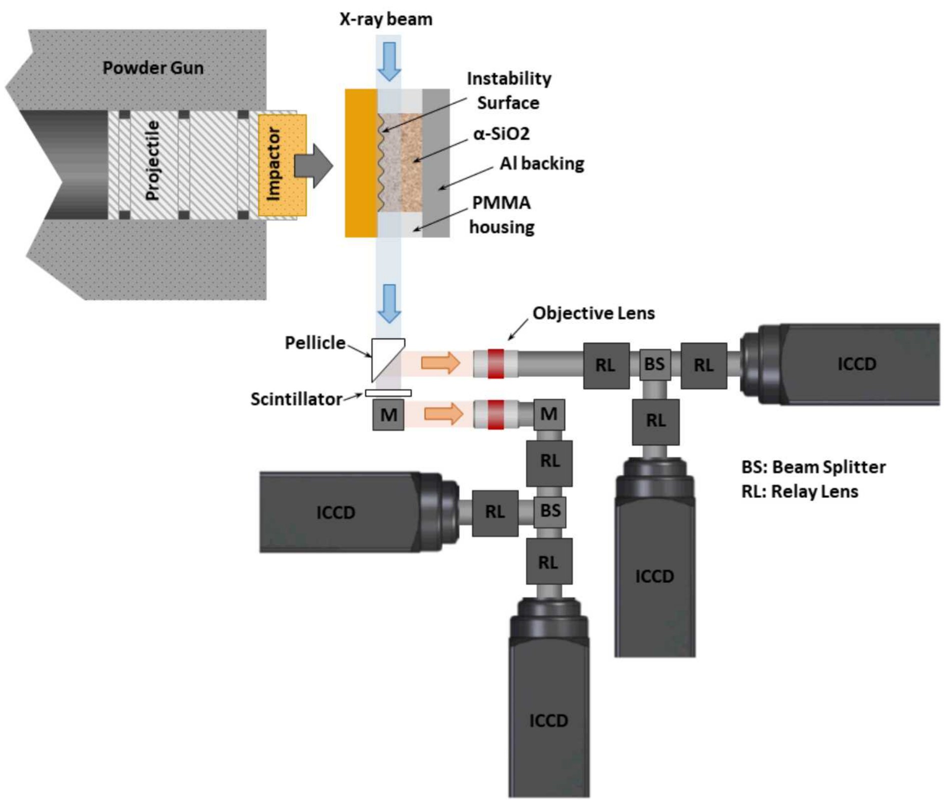

Figure 2-2. Schematic of the experimental assembly utilized at the DCS to capture the jetting inversion process

Initial effort was made to track the entire jet profile and compare with simulation, but as will be described in Section 2.3, it was found that jet length (i.e. peak-to-valley distance of the inverted sine-wave profile) was a simple candidate for model calibration. Thus, importance was placed on capturing said profile in the experimental window.

2.1.3. Modeling Approach

Simulation of the powder target assembly was performed with the Eulerian hydrocode CTH [21]. Due to the inherent symmetry of the impact geometry, mirror boundary conditions were applied at the top and bottom of a 2-D Cartesian mesh, wherein one wavelength of the event is simulated. A schematic of the simulation is shown in Figure 2-3.

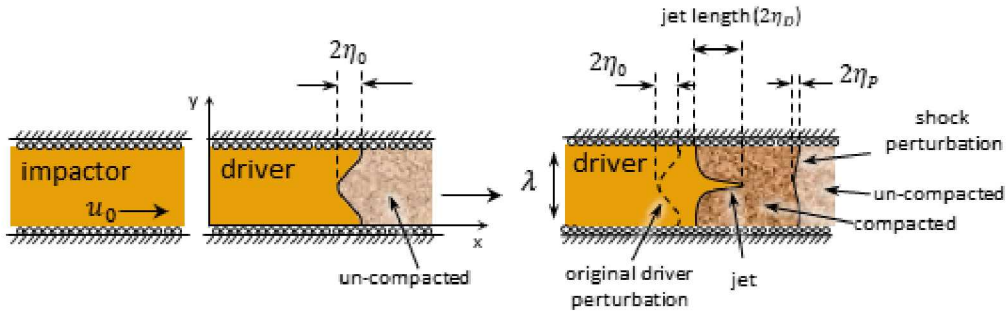

Figure 2-3. Schematic of the RMI simulation of copper driven into porous α-SiO_2

In this format, an initial velocity was applied to a copper impactor, thereby initiating a shock in the copper driver upon impact. Said shock then traversed across the driver thickness and released down via driving a shock front in the α-SiO_2 media, thereby driving compaction. Behind this compaction front, the driver corrugation is designed to invert, thereby promoting Cu jet growth into the compacted α-SiO_2; the jet then subsequently arrested. A Mie-Grüneisen equation-of-state (EOS) overlaid with an elastic-perfectly plastic (EPP) constitutive model was used to describe the Cu material, as defined in Tables 2-1 and 2-2; the constitutive behavior was calibrated in via driving a jet into a hydrodynamic fluid, as described in Appendix A.1. The porous α-SiO_2 media was described as a continuum via the P-α compaction model [22]. Additionally, the pressure-dependent yield surface GEO was used to describe the strength of the α-SiO_2 material, with the shape of the yield surface being the object of calibration via the captured experimental data set.

Table 2-1. EOS parameters used in RMI simulations

Material	EoS	ρ_{00} (g/cc)	P_s (GPa)	n	Co (km/s)	s
α-SiO_2 powder	Sesame 7360	1.55	1.8	2	-	-
Copper	Mie-Grüneisen	8.93	-	-	3.94	1.489
PMMA	Mie-Grüneisen	1.186			2.3	1.75

Table 2-2. Strength model input parameters used in RMI simulation

Material	Model	Y_0 (GPa)	Y_{inf} (GPa)	v	$\frac{dY}{dP}$	T_{melt} (eV)
α-SiO_2 powder	GEO	0.01	9	0.2	0.8	0.13
Copper	EPP*	0.46-0.49	-	0.36	-	-
PMMA	Johnson-Cook**	0.46-0.48	-	0.4	-	-

*EPP model is calibrated from the Cu tamped with D_2O as discussed in Appendix A.
**A = 0.076 GPa, B = .069 GPa, C = 0, n = 1.85, n = 1, Tm = 0.048 eV

As mentioned in Section 2.1.2, the temporal jet length ($2\eta_D$) was used as the parameter for model calibration, so Lagrangian tracers were placed at the initial peak and valley of the perturbation. Additionally, in order to track the perturbation decay [6] of the compaction front in the α-SiO_2, Lagrangian tracers were placed in the horizontal direction (x = 0) along both the initial peak (y = 0) and valley (y = λ/2) of the sinewave. A post-process script was developed to track large pressure differences along the Lagrangian tracer arrays, thereby allowing location of the furthest and least distance travelled portion of the perturbation front, with the difference here-on being defined as the perturbation thickness ($2\eta_P$).

The housing PMMA material and Cu impactor/driver were represented by Mie-Grüneisen equations of state (EOS) as described in Table 2-1. The α-SiO_2 powder was modeled by Sesame 7360, overlaid with a P-α crush model describing the compaction process. The maximum distention parameter α, defined at a pressure P, has the functional form described in Equation 2-2,

$$\alpha = 1 + \left(\frac{\rho_s}{\rho_{00}} - 1\right)\left(\frac{P-P_s}{P_e-P_s}\right)^n \quad \text{(Eq. 2-2)}$$

wherein ρ_s and ρ_{00} represent the crystal and initial porous densities, respectively. The max elastic transition pressure and pressure at which porosity is fully removed from the material are represented in Equation 2-2 by P_e and P_s, respectively. It should be noted that at pressures below P_e, the elastic region of the crush curve is reversible upon release; at pressures greater than P_e, the crush behavior is irreversible. The term elastic does not refer to deviatoric terms in the stress tensor, but rather behavior along the hydrostat. A plot of the Hugoniot for the α-SiO_2 powder in P-v space can be seen in Figure 2-4.

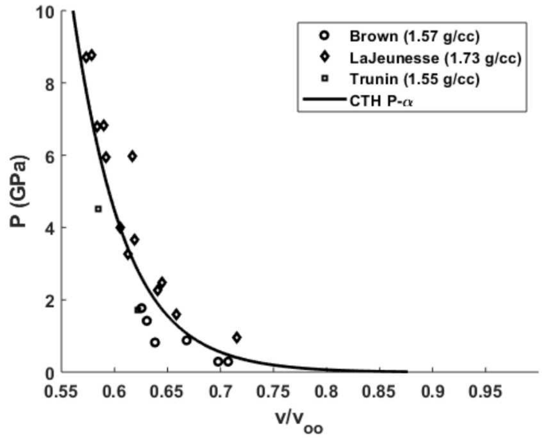

Figure 2-4. P-v of Hugoniot response in α-SiO_2. Data from literature is demonstrated by markers and solid curve represent the Hugoniot used in simulation.

The PMMA material has been overlaid with a Johnson-Cook strength model, with parameters given in Table 2-2. The constitutive behavior of the copper driver is represented by an elastic-perfectly plastic model, which is calibrated via similar experiments wherein jets are driven into a D_2O tamp; this experimental set is described in Appendix A.1. In order to capture the strength response of the α-SiO_2 granular media, a pressure dependent yield surface is overlaid onto the SESAME/P-α EOS, which is described by Y in Equation 2-3.

$$Y = Y_\infty + (Y_0 - Y_\infty) exp\left[-\frac{dY}{dP}\frac{P}{Y_\infty - Y_0}\right] \qquad \text{(Eq. 2-3)}$$

As can be seen from the form of Equation 2-3, the yield strength Y varies from a zero-pressure strength Y_0, to a maximum pressure strength of Y_∞; in this case, Y_0 has been selected to be negligibly small, and Y_∞ is selected to reflect the elastic limit of the corresponding solid material. The shape of the yield surface is governed by the parameter $\frac{dY}{dP}$, with increasing values of $\frac{dY}{dP}$ resulting in increased strength at a given pressure. It is this $\frac{dY}{dP}$ parameter that is being calibrated from the experiment using an optimization scheme of the simulation. As an aside to the interested reader, a first pass at an approximate yield stress is developed via applying an EPP model to the granular media; upon matching the jet length as a function of time, the yield strength is used to estimate a starting point for the $\frac{dY}{dP}$ parameter in the optimization scheme. Additionally, the yield surface is softened at elevated temperature states.

2.2. Results/Discussion

In efforts to calibrate the pressure-dependent GEO model applied to α-SiO_2, several Richtmyer-Meshkov experiments were performed within a drive pressure range of 4-10 GPa as described in Section 2.1.2. Wavenumbers of the corrugated surface in the shots were selected *a priori* via simulation to be between 1-2 and are displayed with relevant shot info in Table 2-3.

The diagnostic implemented in this experimental effort is the capture of PCI radiography via the eight-frame camera system with interframe time of 153.4 ns. The temporal resolution corresponds to the electron bunch length in the APS storage ring, which is roughly 50 ps. The spatial resolution is defined by the objective magnifier employed, and in this experimental sequence, is roughly 2.59 μm/pixel.

The primary dimension of interest in these experiments is the peak-to-valley distance of the evolving jet ($2\eta_D$), which is demonstrated the schematic of Figure 2-3. An example of an experimental jet evolution can be seen in Figure 2-5, which demonstrates a Cu symmetric impact of 2.0 km/s wherein the rear corrugated surface of the driver possesses a wavelength and wavenumber of 1 mm and 1, respectively. As one can see in the experimental image sequence, this impact event results initially in a shock wave being drive into the α-SiO_2 granular material, thereby promoting compaction. Following within this compaction regime, the corrugated surface in this experiment is driven to invert in a RMI fashion, wherein the initial sinewave peaks become valleys and the initial valleys become peaks. It should be noted that in literature, these newly formed valleys are traditionally called bubbles and the newly formed peaks are called spikes; the current work calls these peaks "jets". Below the experimental sequence, there is also an example material image sequence generated from hydrocode simulation that is locked time correlated to the experiment. Clearly the inversion process can be seen in the hydrocode, being very similar to the experiment. Additionally, the third row of Figure 2-5 demonstrates the compaction wave that is developed in the hydrocode simulation; this sequence is also locked in frame time to the experimental sequence, demonstrating the evolution of the compaction wave, which inverts with the corrugated surface.

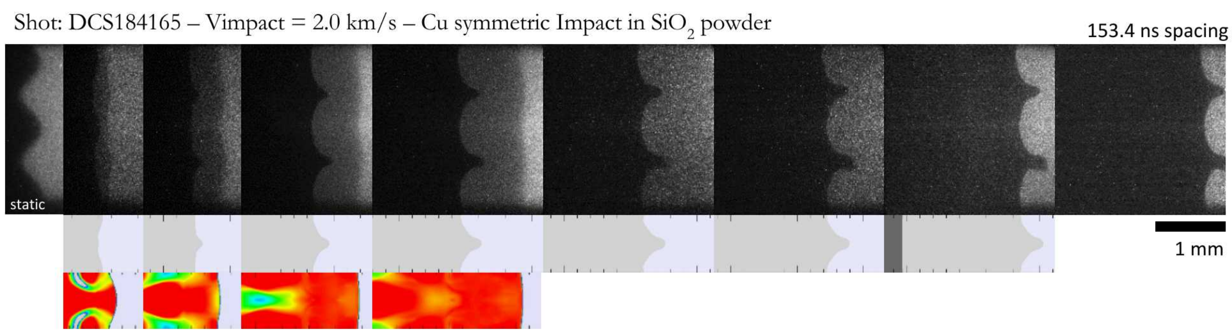

Figure 2-5. Sequence of corrugation inversion seen from experiment (top) and hydrocode simulation (middle). The compaction front imaged in the experiment is also demonstrated via simulation (bottom)

Capturing of the image sequence is then analyzed and the jet length ($2\eta_D$) as well as the perturbation front thickness ($2\eta_P$) is tracked and digitized for each of the image sequences. An example of this capture can be seen in Figure 2-6 (identical experiment to the data shown in Figure 2-5) for both the jet length and perturbation front thickness, which are demarcated by the diamonds and circles respectively. In this scheme, positive values are taken as the distance between the peak-valley before inversion, and negative values represent the distance after inversion, wherein there is the newly defined bubble and jet. As elucidated in Figure 2-5, and demonstrated in the plot of Figure 2-6, it is apparent that both perturbation and the corrugated surface invert in this experiment. Immediately apparent is the large difference in numerical amplitude between the perturbation front thickness and the resulting jet length. The jet length provides a much greater number of pixels as compared to the perturbation front thickness, thereby allowing for greater sensitivity in the model calibration. It should also be pointed out that although it is difficult to see the steady-state nature of the perturbation front, it does appear that the jet length has arrested, thereby achieving a steady state value. This arrested jet-length at later times is ideal, as it removes the need for time correlation of the simulation to the experiment. Additionally, due to the slower nature of the evolving jet as compared to the compaction front, it is possible to catch more frames within the imaging field of view during a single experiment.

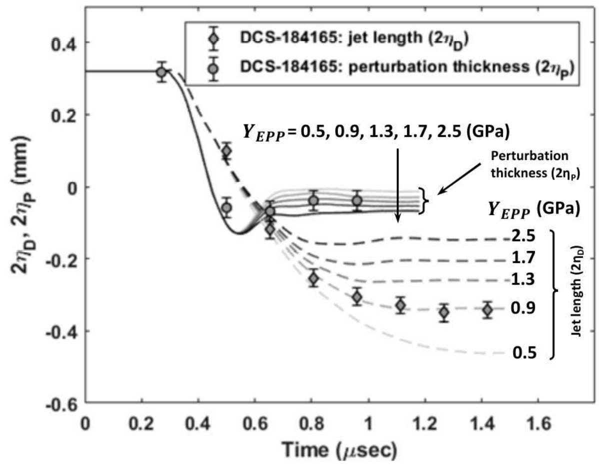

Figure 2-6. Resulting jet length and perturbation thickness as a function of time

On top of the experimental data demonstrated in Figure 2-6, the output perturbation front thickness and jet length as simulated via hydrocode are also overlaid on the plot. Several values of the yield strength have been selected, using an EPP model as a first estimation of the α-SiO_2 yield strength. Although crude, using EPP allows for an estimate of the strength exhibited by the α-SiO_2 powder at a specific drive pressure, which is then further tuned with a full pressure-dependent yield surface. As can be seen in Figure 2-6, there is insufficient resolution in the experimental data to parse between a strength of 0.5 and 2.5 GPa using the perturbation front thickness. It is indeed though possible to estimate the strength of the granular material within 0.2 GPa using the jet length, as the measured jet length is much greater in amplitude than the perturbation front thickness, being roughly 0.35 mm and 0.03 mm, respectively. It should also be noted that the effect of the Cu driver strength must be taken into account for the simulation, and thus Appendix A.1 demonstrates the calibration of the Cu strength at similar drive pressures and strain-rates via tamping the Cu driver with the liquid D_2O.

Table 2-3. RMI shot parameters

Shot #	Impactor Mat	Wave number	Drive Pressure (GPa)	Y (GPa)
19-1-029	Cu	1	6.75	2.4
19-1-030	Ta	1	10	0.5
19-1-037	Cu	2	4.5	2.7
18-4-165	Cu	1	9.5	0.9

This same approach is taken for estimating the strength of the α-SiO_2 yield strength at the drive velocities listed in Table 2-3. The resulting strength values at specific drive pressures are demonstrated in Figure 2-7, being demarcated by blue traingles. It must be pointed out that the drive pressure is inherently a function of the selected strength model, and must be converted from drive stress if thought of in a 1-D experimental geometry. As can be seen in Figure 2-7, the four experimental data points demonstrate a depreciating value of strength with increasing drive pressures, which is to be expected for a granular material that approaches melt due to the large energy increase created from the volume collapse due to shock loading. This depreciating yield surface has been initially fitted with a Drucker-Prager cap model, which is defined in Equation 2-4, wherein the strength Y represents the pressure dependent yield strength of the material at a specific drive pressure, P. Such a cap model is well established in literature for granular media [1, 2], being used in a range of data analysis (e.g. blast loading [23], projectile penetration [24] and pharmaceutical pill compact formation [25]) with the cap yield surface Y_c being a function of pressure P, which is defined in Equation 2-4.

$$F_c = \sqrt{[P - P_a]^2 + \left[\frac{RY_c}{1+\alpha-\alpha/cos\beta}\right]^2} - R(d + P_a tan\beta) = 0 \quad \text{(Eq. 2-4)}$$

Assuming that α = 0 and d = 0, Equation 2-4 can be simplified and rearranged to Equation 2-5,

$$Y_c = \sqrt{\left(\frac{P-P_a}{R}\right)^2 + (Ptan\beta)^2} \qquad \text{(Eq. 2-5)}$$

Within Equation 2-5, the fitting parameters have been selected to be R = 2.2, β = 32^0, and P_a = 10 GPa. Additionally, a traditional Drucker-Prager yield curve has been suggested for pressures below 4 GPa, being defined by Equation 2-6.

$$Y_1 = Ptan\beta \quad \text{(Eq. 2-6)}$$

On top of the experimental data and resulting Drucker-Prager capped yield surface captured in the current work, experimental data from pressure-shear experiments on silica sand [3, 4] have also been overlaid, being demarcated by the gray circles and diamonds near the origin of the plot. Additionally, simulation of the pressure-shear experiment by LaJuenesse led to artificial data points that are demarcated by the solid and open black circles within Figure 2-7. Although not within the scope of this report, it is important to note that pressure-shear experiments are apt to under-predict the yield behavior of the sample material; there exists a fine interplay between ensuring drive anvils remain elastic, no slippage occurs between the anvils and sample, and the sample fully plastically yields, which can result in a "softening" of the exhibited yield behavior (e.g. sample may slip or the sample may not fully yield).

In efforts to generate a yield surface allowing for simulation of the entire range in pressure explored up to 10 GPa, the GEO model has been calibrated in the hydrocode CTH with parameters shown in Table 2-2. The resulting profile can be seen in Figure 2-7 and is demarcated by the blue solid curve. Initially, within the low pressure regime up from 0-4 GPa, there is a monotonic increase in the yield strength as a function of pressure, which roughly follows the initial Drucker-Prager region Y_1 defined in Equation 2-6. At increasing drive pressures, increased levels of thermal heating are experienced within the granular media due to compaction; such a behavior softens the yield curve, resulting in a decrease of the surface to zero strength at a drive pressure of roughly 10 GPa. It can be seen that the GEO yield surface in Figure 2-7 follows the Drucker-Prager surface reasonably well, and it is this GEO surface that is to be used in the Section 3, which will act as a model validation study.

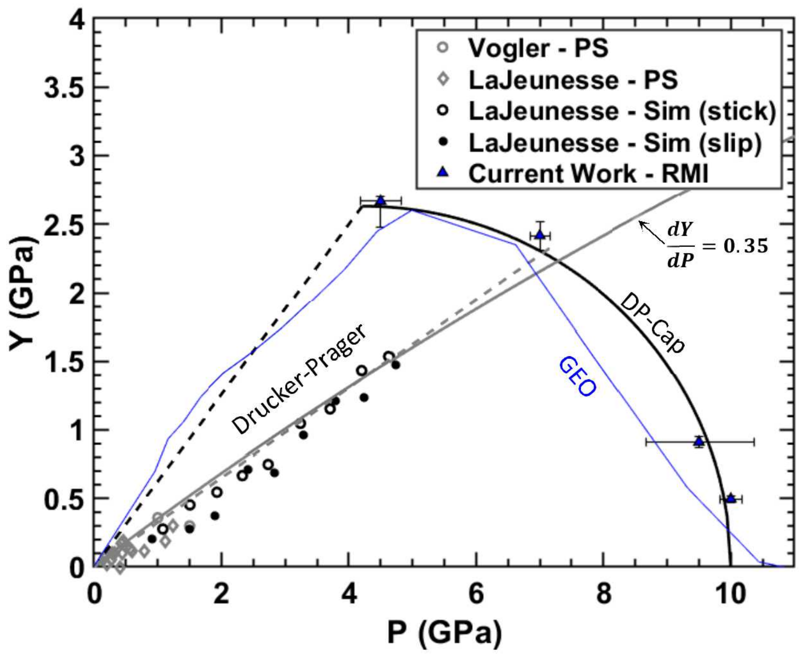

Figure 2-7. GEO and Drucker-Prager yield surfaces fitted to the α-SiO_2 RMI data ranging up to 10 GPa

3. MACH LENS

3.1. Experimental

3.1.1. Materials

Several Mach lens drive experiments were performed at the DCS and modelled via hydrocode with two goals in mind. First, so as to compare two reasonably impedance matched distended materials possessing vastly different ambient strength values; α-SiO_2 (identical to that shown in Section 2.1) and nearly pure (99.99%) Al (Atlantic Equipment Engineers) powders were selected as candidates for this non-planar compaction study. Second, in efforts subject the α-SiO_2 GEO constitutive model calibrated in Section 2 to a validation case study. Powders in these experiments were dry-sieved to a particle size less than roughly 20 microns and had a nominal tap density of 1.55 g/cm^3. Morphology of the Al was reasonably spherical in nature, while the SiO2 was highly faceted, which is demonstrated in Figures 3-1 and 2-1, respectively.

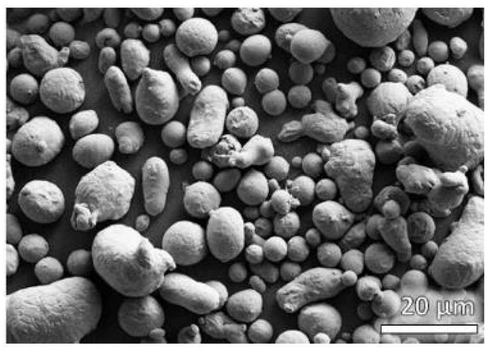

Figure 3-1. SEM of sample Al material

3.1.2. Experimental Setup

Granular media was loaded in an 8 mm long PMMA cylindrical housing having an outer diameter of 8 mm and an inner diameter of 800 µm capped on both ends with thin PMMA discs. Loaded powder densities were nominally 1.55 g/cc for both Al and α-SiO_2 powders (approximately 57% and 58% of theoretical max density, respectively). A schematic of the capsule geometry can be seen in Figure 3-2(a). Sample assemblies were then loaded into the DCS gun system depicted in Figure 3-2(b) and impacted by either LiF or Al flyers at velocities of ~1 – 2.5 km/s. Coupled to the impact time of the flyer and target, the shock evolution in the housing/core was illuminated by a 23.1 keV pulse-separated X-ray beam generated from the U17 undulator placed within the storage ring of the Advanced Photon Source at Argonne National Laboratory. An ultra-fast imaging system was implemented to capture the wave-profile history in the sample region of interest via phase contrast imaging (PCI), being temporally coupled to the X-ray bunch arrival at an interframe spacing of 153.4 ns. The housing material and geometry were selected so as to drive a Mach lens in the inner distended media, via the nominally planar shock in the higher impedance PMMA housing material, which is depicted in Figure 3-2(c).

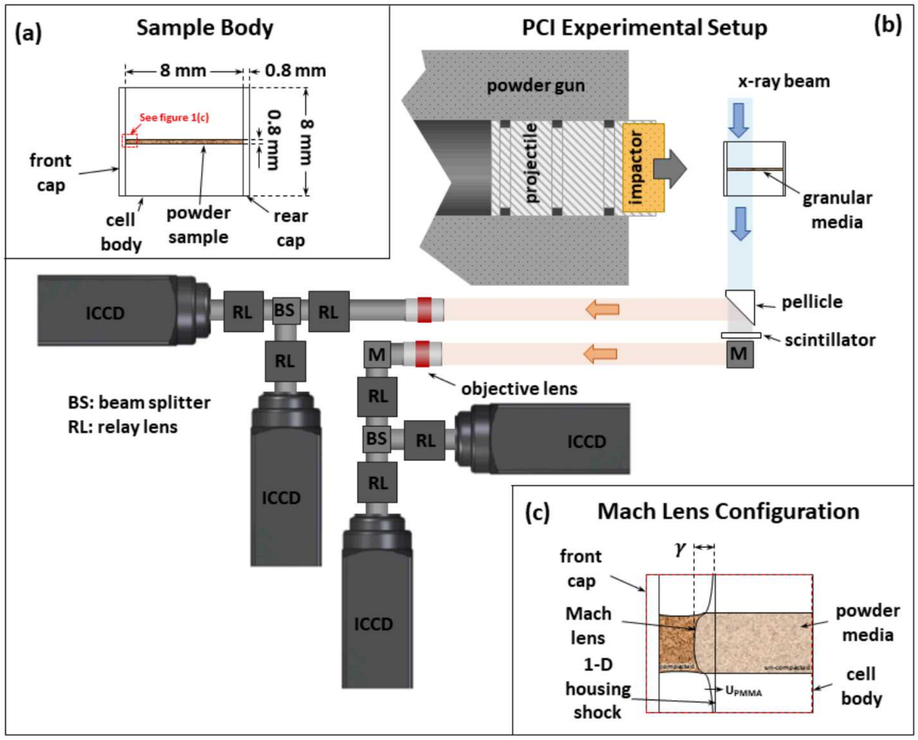

Figure 3-2. Schematics of (a) sample body geometry, (b) DCS and sample assembly including flyer/launcher, sample, and diagnostic PCI system, (c) enlarged view of powder column Mach lens profile

3.1.3. Modeling Approach

Simulation of the powder column evolution was performed with the Eulerian hydrocode CTH. Due to the inherent symmetry of the impact geometry, a 2-D cylindrical boundary condition was employed. A schematic of the simulation is shown in Figure 3-3. In order to track the Mach lens thickness and resulting state variables behind the propagating wave, Lagrangian tracers were placed within the powder core (r = 0), at the core-housing interface (r = 400 um), and at multiple radial locations along the cell body. The housing PMMA material, Al/LiF drivers were each represented by a Mie-Grüneisen equation of state (EOS), with the PMMA material also being overlaid with a Johnson-Cook strength model. The Al powder was modelled with Sesame 3700 and the α-SiO_2 powder was modeled by Sesame 7360; both Al and α-SiO_2 were overlaid with a P-α crush model describing the compaction process. The resulting P-v curve for Al can be seen in Figure 3-4, while the compaction curve for α-SiO_2 was demonstrated in Figure 2-4.

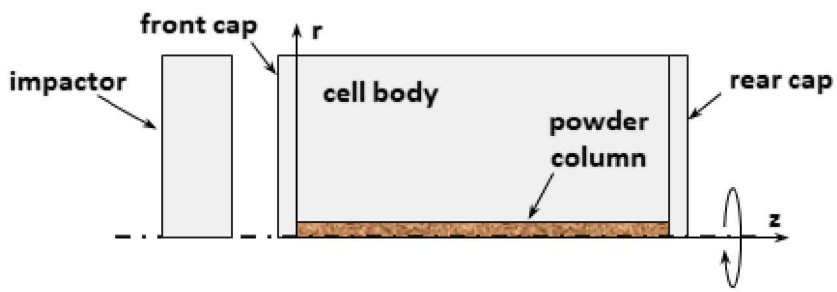

Figure 3-3. Schematic of Mach lens simulation

As demonstrated in Figure 3-4, the compaction response of porous Al has a negligible crush pressure and is demarcated by the blue curve and magenta markers as generated from analytical Mie-Grüneisen EOS and the Sesame 3700 EOS overlaid with the P-α compaction model, respectively. Additionally, Figure 3-4 demonstrates experimental 1-D shockwave data at similar pack densities. At low drive pressures, the Sesame 3700 P-α compaction response coincides with the Mie-Grüneisen response, but at elevated drive pressures of roughly 15 GPa, there is deviation in the response due to increased temperature from the compaction process; the Sesame 3700 P-α compaction response appears to line up well with the experimental data at elevated drive pressures.

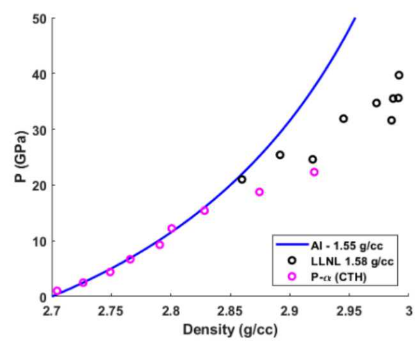

Figure 3-4. P-v response of Al powder used in Mach lens experiments

Additionally, for the α-SiO_2 powder, the calibrated yield surface generated throughout the work in Section 2 and demonstrated in Figure 2-7 has been input directly into the Mach lens simulations; no changes were made to the yield surface for these simulations, as the Mach lens experiments on the α-SiO_2 material act as a model validation study of the yield surface calibration. EOS parameters implemented for all Mach lens experiments can be seen in Table 3-1.

Table 3-1. EOS parameters used in Mach lens simulations

Material	EoS	ρ_{00} (g/cc)	P_s (GPa)	n	Co (km/s)	s
α-SiO_2 powder	Sesame 7360	1.55	1.8	2	-	-
Al powder	Sesame 3700	1.55	0.01	2	-	-

Material	EoS	ρ_{00} (g/cc)	P_s (GPa)	n	Co (km/s)	s
PMMA	Mie-Grüneisen	1.186	-	-	2.3	1.75
Al Impactor	Mie-Grüneisen	2.707	-	-	5.25	1.37
LiF Impactor	Mie-Grüneisen	2.638	--	-	5.15	1.35

Table 3-2. Strength model input parameters used in RMI simulation (identical to Table 1-2, but shown again to reiterate the validation nature of the Mach lens α-SiO₂ shots)

Material	Model	Y_0 (GPa)	Y_{inf} (GPa)	v	$\frac{dY}{dP}$	T_{melt} (eV)
α-SiO_2 powder	GEO	0.01	9	0.2	0.8	0.13
PMMA	Johnson-Cook**	0.46-0.48	-	0.4	-	-

**A = 0.076 GPa, B = .069 GPa, C = 0, n = 1.85, n = 1, T_m = 0.048 eV

3.2. Results/Discussion

Mach lens experiments of low impedance powder material housed in a higher impedance solid housing has been performed to subject the distended media to a non-planar loading condition with a range in experienced pressures within the powder column; said non-planar loading environment inherently exacerbates strength effects, thereby allowing for an exemplary model validation tool, as the inherent pressure range present in the Mach lens event provides an ideal model validation framework. An example of said pressure range is demonstrated in Figure 3-5, wherein a 1.55 g/cc core of Al powder housed in PMMA was impacted at 1.7 km/s via LiF. At the top right of the figure can be seen a captured PCI radiograph, and directly below it can be seen a density viewgraph as predicted from hydrocode simulation. Upon impact of the LiF with the PMMA body, a 1-D shock in the PMMA is generated; said shock propagates in a planar fashion except in the vicinity in the Al powder core. The initial planar shock in the PMMA cap along the powder core drives a planar shock in the Al powder, which is almost immediately affected by the shock in the housing; the planar shock in the surrounding PMMA the powder core releases down into the Al powder in a radial fashion. As the shock in the PMMA moves faster than the intial planar shock in the Al powder, the PMMA shock quickly overruns the initial planar shock in the Al powder, and a concentric Mach lens is then formed in the Al powder. This lens shape profile can be seen in both the experimental radiograph and simulation viewgraph on the right of Figure 3-5. In order to better demonstrate the resulting spatial and temporal pressure history of powder within the PMMA housing, two lineouts are plotted in Figure 3-5, resulting from Lagrangian tracers along the center of the powder core, and near the core-housing interface, being demarcated by solid and dashed lines, respectively. Looking at the pressure versus axial location of the lineouts, several features are immediately apparent. First, near the leading edge of the wave in both the core and interface, there exists an initial pressure spike felt by porous media. The pressure spike at the core is greater than the interface; this is because the axial velocity of the shock wave is identical in both locations, but the core material experiences a jump across a normal, whereas near the interface experiences a jump across an oblique wave. The amplitude of the pressure spike in the core is identical to the pressure that would be experience by the powder material if a planar shock was driven in the powder material at the same shock velocity of the Mach lens velocity (shock velocity of the normal shock driven in the PMMA). Additionally, after the initial pressure spike is felt by the porous material, the porous media releases down to a steady state pressure that is identical in both the core and interface; this steady state pressure is identical to the normal shock pressure experienced by the PMMA housing. Finally, the initial 1-D shock developed in the powder material is quickly overran by the Mach lens, and for the Al powder, occurs within ~1-2 radii from the PMMA cap and Al powder interface.

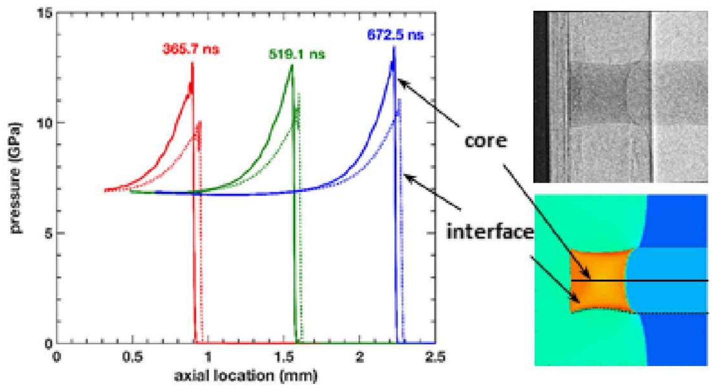

Figure 3-5. Pressure evolution in Mach lens experiment along core and interface for 1.55 g/cc Al powder within a PMMA housing impacted with LiF at 1.7 km/s

In order to provide model validation of the α-SiO_2 strength model developed in Section 2, the calibrated GEO yield surface has been directly applied to the α-SiO_2 powder within the Mach lens experiments. In order to demonstrate the effect of including a strength model on the resulting Mach lens profile, Figure 3-6 depicts a comparison between captured PCI radiographs of α-SiO_2 powder being driven by PMMA (top), as well as hydrocode simulation with and without strength overlaid (bottom and middle, respectively). Immediately it is apparent that in contrast to the porous Al response, α-SiO_2 exhibits quite a different response to the Mach lens environment, yielding a much longer distance from the back of the Mach lens to the normal shock in the PMMA (γ). From the experimental radiographs, it can be seen that for the impact velocity of the LiF into the PMMA impact cap at 1.131 km/s, when the normal shock in the α-SiO_2 is overran by the Mach lens generation, rather than a "u" shaped profile, the response appears to exhibit a "v" shaped profile. Comparing the time synchronized pressure fields demonstrated in Figure 3-6, the change from the "u" to "v" profile is due to the inclusion of the pressure-dependent GEO strength model described in Section 2.

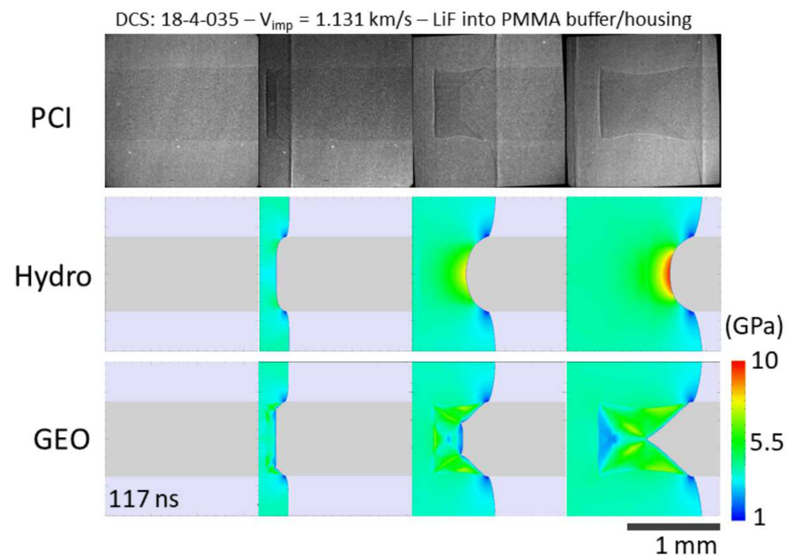

Figure 3-6. α-SiO_2 powder Mach lens evolution seen in experiment (middle), no-strength (middle), and GEO (bottom)

In order to check the efficacy of the GEO strength model in α-SiO_2 at range of drive pressures, several Mach lens experiments have been performed, and the resulting measured Mach lens thickness (γ) histories are demonstrated in Figure 3-7 via circular markers. For each shot, the transient Mach lens length appears to increase from zero (initial planar shock) to a roughly steady state value. With increasing shot velocities, it can be seen that the Mach lens length decreases. Within Figure 3-7, simulation of the resulting Mach lens length is also depicted both with and without the GEO strength model, represented by solid and dashed curves, respectively. Several things of note can be seen in the figure. Firstly, at lower impact velocities, it is clearly apparent that there exists a large difference in Mach lens length when comparing the simulations with and without strength. As the impact velocity increases, this apparent difference decreases, and becomes indiscernible at the listed impact velocity of 2.45 km/s. This is to be expected, as the relative difference between the deviatoric stresses present and the drive pressure decreases as the drive pressure increases as defined by the GEO model calibration. Secondly, it can be seen that the experimental values are simulated remarkably well with the RMI calibrated yield surface, especially at the lower impact velocities displayed within Figure 3-7. At the highest simulated impact velocity of 2.45 km/s, the match between experiment and simulation starts to deviate, demonstrating that at the highest simulated drive pressures, there may still exist some strength in the porous compaction response, although the GEO model assumes that the strength at ~10 GPa goes to zero. It is also important to note that the time matched experimental data and simulation curves in Figure 3-7 have been arbitrarily time shifted together so as to visualize multiple data sets/simulations on the same plot.

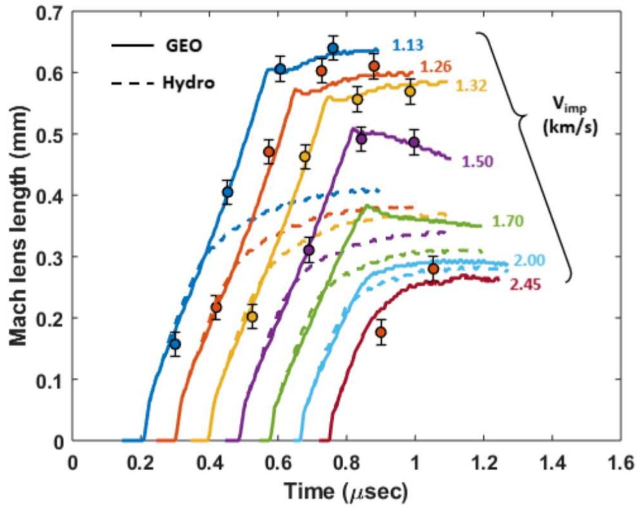

Figure 3-7. Mach lens length of α-SiO_2 powder at a variety of drive velocities for experiment (markers), no-strength simulations (dotted curves) and calibrated GEO strength simulations (solid curves)

4. CONCLUSIONS

In efforts to assess the strength of α-SiO_2 powder subjected to shock loading, a growth and arrest Richtmyer-Meshkov instability was implemented. In such an environment, the porous media was compacted to a defined pressure state and subsequently deformed via Cu jets driven into the compacted powder. The jet shape/length was tracked via time-resolved radiography using a synchrotron light source. Numerical simulation of the event was then performed, and a pressure-dependent yield surface was optimized to fit the experimental data of shots driving specific pressure states between 4-10 GPa. Additionally, in order to provide model validation, a set of Mach lens experiments were performed, and subsequently simulated using the RMI calibrated pressure-dependent yield surface. Good agreement was found between the Mach lens experiments and simulations when using the calibrated strength model, giving confidence in the fitted constitutive response. Furthermore, the Mach lens experiments were modelled in the absence of a yield surface (purely hydrodynamic) resulting in large variation between simulated Mach lens shape profile when implementing strength; such a variation points to the importance of including a proper yield surface when assessing α-SiO_2 data involving shock pressures in the regime up to 10 GPa.

REFERENCES

[1] J. Bardet, "BOUNDING SURFACE PLASTICITY MODEL FOR SANDS," *J. Eng. Mech.,* vol. 112, no. 11, pp. 1198-1217, 1986.

[2] Y. Hammi, T. W. Stone, B. Paliwal, M. F. Horstemeyer and P. G. Allison, "Smooth Yield Surface Constitutive Modeling for Granular Materials," *J. Eng. Mater. Technol,* vol. 139, no. 1, p. 011010, 2016.

[3] J. W. LaJeunesse, Dynamic Behavior of Granular Earth Materials Subjected to Pressure-Shear Loading, Milwakee: Marquette University, 2018.

[4] T. J. Vogler, C. S. Alexander, T. F. Thornhill and W. D. Reinhart, "Pressure-shear experiments on granular materials," SAND2011-6700, 2011.

[5] R. Clifton and R. Klopp, "Pressure-shear plate impact testing," in *Metals Handbook*, Metals Park, American Society for Metals, 1985, pp. 230-239.

[6] T. Vogler, "Shock Wave Perturbation Decay in Granular Materials," *Journal of dynamic behavior of materials,* vol. 1, pp. 370-387, 2015.

[7] A. Sakharov, R. Zaidel, V. Mineev and A. Oleinik, "Experimental investigation of the stability of shock waves and the mechanical properties of substances at high pressures and temperatures," *SOVIET PHYSICS-DOKLADY,* vol. 9, no. 12, pp. 1091-1094, 1965.

[8] V. Mineev and R. Zaidel, "THE VISCOSITY OF WATER AND MERCURY UNDER SHOCK LOADING," *SOVIET PHYSICS JETP,* vol. 27, no. 6, p. 874–878, 1968.

[9] L. Laine and A. Sandvik, "DERIVATION OF MECHANICAL PROPERTIES FOR SAND," in *Proceedings of the 4th Asia-Pacific Conference on Shock and Impact Loads on Structures*, Singapore, 2001.

[10] M. Grujicic, B. Pandurangan, J. Summers, B. Cheeseman, W. Roy and R. Skaggs, "Application of the modified compaction material model to the analysis of landmine detonation in soil with various degrees of water saturation," *Shock and Vibration,* pp. 79-99, 2008.

[11] G. Dimonte, G. Terrones, F. J. Cherne, T. C. Germann, V. Dupont, K. Kadau, W. T. Buttler, D. M. Oro, C. Morris and D. L. Preston, "Use of the Richtmyer-Meshkov Instability to Infer Yield Stress at High-Energy Densities," *Physical Review Letters,* vol. 107, no. 26, p. 264502, 2011.

[12] A. He, J. Liu, C. Liu and P. Wang, "Numerical and theoretical investigation of jet formation in elastic-plastic solids," *Journal of Applied Physics,* vol. 124, p. 185902, 2018.

[13] K. Mikaelian, "Richtmyer-Meshkov instability with viscosity or strength," LLNL-JRNL-557777, Livermore, 2012.

[14] A. Mikhailov, "Hydrodynamic instabilities in solid media - from the object of investigation to the investigation tool," *Physical Mesomechanics,* vol. 10, no. 5-6, pp. 265-274, 2007.

[15] A. Piriz, Y. Sun and N. Tahir, "Hydrodynamic instability of elastic-plastic solid plates at the early stage of acceleration," *Physical Review E,* vol. 91, p. 33007, 2015.

[16] M. B. Prime, W. T. Buttler, M. A. Buechler, N. A. Denissen, M. A. Kenamond, F. G. Mariam, D. M. Oro, D. W. Schmidt, J. I. Martinez, J. B. Stone, D. Tupa and W. V. McNeil, "Estimation of Metal Strength at Very High Rates Using Free-Surface Richtmyer-Meshkov Instabilities," *Journal of Dynamic Behavior of Materials,* vol. 3, no. 2, pp. 189-202, 2017.

[17] W. T. Buttler, D. M. Oró, D. L. Preston, K. O. Mikaelian, F. J. Cherne, R. S. Hixson, F. G. Mariam, C. Morris, J. B. Stone, G. Terrones and D. Tupa, *Journal of Fluid Mechanics,* vol. 703, pp. 60-84, 2012.

[18] M. Brouillette, "THE RICHTMYER-MESHKOV INSTABILITY," *Annu. Rev. Fluid Mech,* vol. 34, pp. 445-468, 2002.

[19] R. HOLMES, G. DIMONTE, B. FRYXELL, M. GITTINGS, J. GROVE, M. SCHNEIDER and Q. ZHANG, "Richtmyer–Meshkov instability growth: Experiment, simulation and theory," *Journal of Fluid Mechanics,* vol. 389, pp. 55-79, 1999.

[20] S. Luo, B. Jensen, D. Hooks, K. Fezzaa, K. Ramos, J. Yeager, K. Kwiatkowski and T. Shimada, "Gas gun shock experiments with single-pulse x-ray phase contrast imaging and diffraction at the Advanced Photon Source," *Review of Scientific Instruments,* vol. 83, p. 073903, 2012.

[21] J. McGlaun, S. Thompson and M.G.Elrick, "CTH: A three-dimensional shock wave physics code," *International Journal of Impact Engineering,* vol. 10, no. 1-4, pp. 351-360, 1990.

[22] W. Herrmann, "Constitutive equation for the dynamic compaction of ductile porous materials," *Journal of Applied Physics,* vol. 40, pp. 2490-2499, 1969.

[23] G. Lu and M. Fall, "State-of-the-Art Modelling of Soil Behaviour Under Blast Loading," *Geotech Geol Eng,* vol. 36, pp. 3331-3355, 2018.

[24] M. Forrestal and V. Luk, "PENETRATION INTO SOIL TARGETS," *Int. J. Impact Engineering,* vol. 12, no. 3, pp. 427-444, 1992.

[25] L. Han, J. Elliott, A. Bentham, A. Mills, G. Amidon and B. Hancock, "A modified Drucker-Prager Cap model for die compaction simulation of pharmaceutical powders," *International Journal of Solids and Structures,* vol. 45, pp. 3088-3106, 2008.

[26] M. Prime, "Exploiting the Unique Capabilities of Richtmyer-Meshkov Instability Strength Measurements at Extreme Strain Rates," in *21st Biennial Conference of the APS Topical Group on Shock Compression of Condensed Matter* , Portland, 2019.

APPENDIX A.

A.1. RMI of OFHC Copper into D_2O

In efforts to capture the yield behavior of the copper driver used for the RMI α-SiO_2 shots described in Section 2, it was desired to run a set of RMI experiments at similar drive conditions, but jetting into a hydrodynamic fluid so as to remove the effect of strength of the tamp material. As such, deuterium oxide (D_2O) was selected as a tamp material. A schematic of the experimental setup can be seen in Figure A-1, wherein the capsule traditionally used in the α-SiO_2 shots is filled with D_2O.

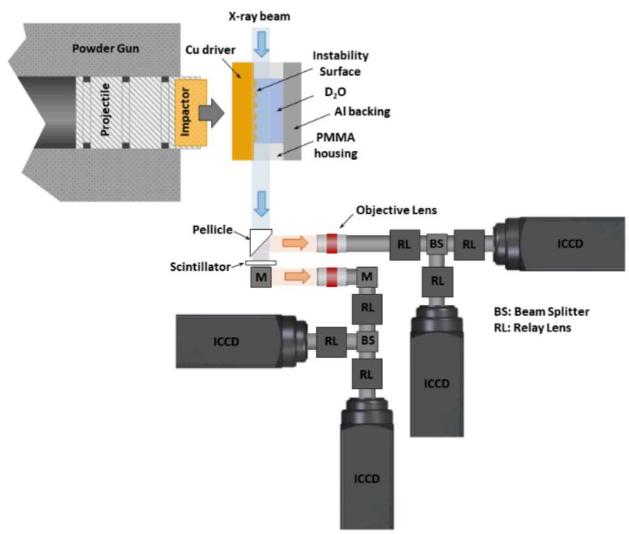

Figure A-1. Experimental setup for RMI tamped via D_2O

A schematic of the instability even can be seen in Figure A-2, demonstrating an event very similar to that described in Section 2.1. In this scenario, a Cu or Ta flyer is ran into a Cu driver, generating a shock in the driver. This shock then traverses across the Cu thickness and releases down off of the heavy water interface. A shock is generated in the D_2O, which quickly attenuates to a planar wave due to the hydrodynamic behavior of the D_2O (which is inherently why such an experiment was devised). With an appropriate selection of drive pressure and corrugation wavenumber, a Cu jet is then driven into the D_2O. Tracking of this jet is performed with the PCI radiography, as well as PDV (although not discussed in this report).

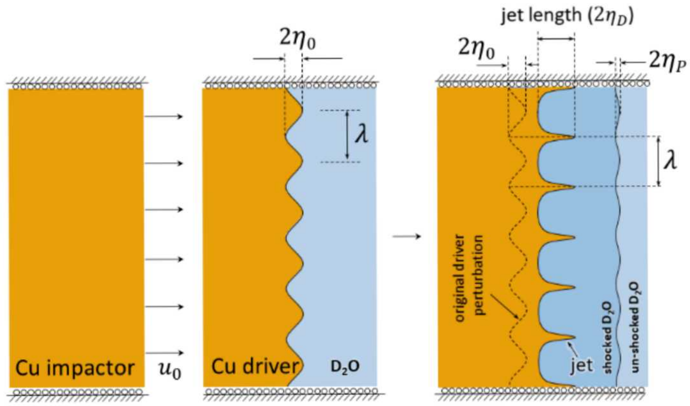

Figure A-2. Schematic of the tamped RMI inversion process

An example of the jet evolution from experiment can be seen in Figure A-3, wherein a Ta driver impacts the Cu target at 1.7 km/s. The target corrugation wavenumber was selected to be 0.5 *a priori*, allowing for inversion, growth, and subsequent arrest within the field of view.

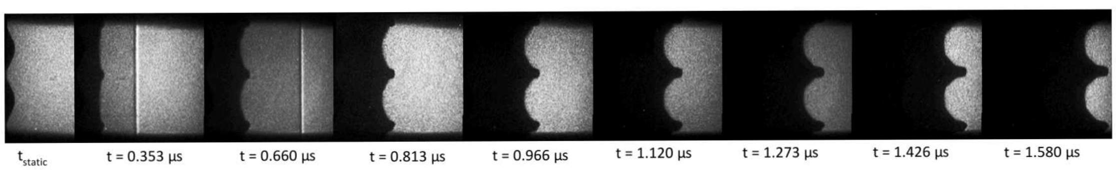

Figure A-3. Experimental data sequence of an RMI event with a Cu driver and D_2O tamping material

The jet evolution from a 1.023 km/s symmetric Cu impact can be seen in Figure A-4, wherein the jet length and perturbation front thickness are plotted as a function of time and demarcated by circular and diamond markers, respectively. Of first to note is that the perturbation front flattens and becomes planar (similar to Figure A-3); additionally, the perturbation front thickness from hydrocode simulation is overlaid in Figure A-4, also damping to a flattened/planar wave. Second to note is the growth and arrest of the jet length demonstrated from the experimental markers in Figure A-4; hydrocode simulation is also overlaid using an elastic-perfectly plastic yield strength model (demonstrated to function well at a specific strain-rate and drive pressure [26]). At the drive pressure of the shot shown in Figure A-4 (3.4 GPa), the resulting yield stress of ~0.48 GPa is calibrated.

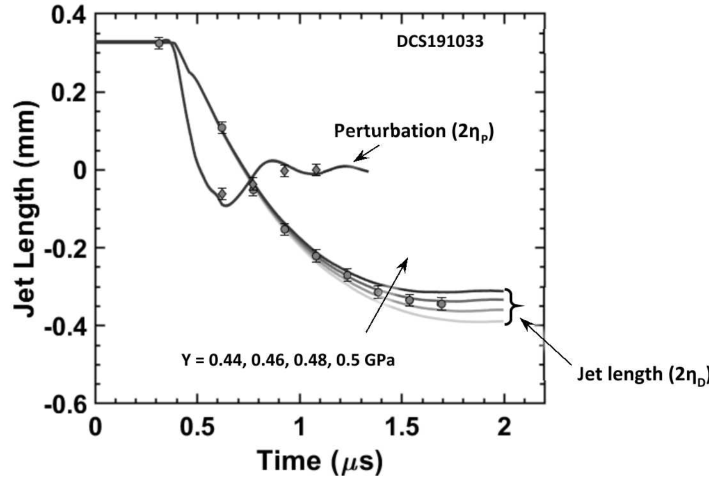

Figure A-4. Appendix Figure Caption

The same process has been performed for three experiments ranging between ~3-10 GPa, and are demonstrated by the blue triangle markers in Figure A-5. It is this trend in yield strength that is included in the simulations of α-SiO_2 discussed in Section 2.

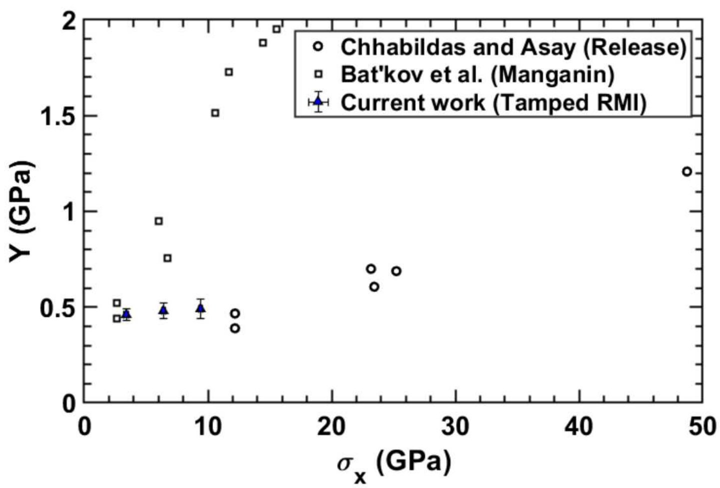

Figure A-5. Appendix Figure Caption

A.2. Illumination of Damage within High-Strength Alloys in Abnormal Mechanical Environments

Academic Alliance
Brett Sanborn[1], Priya Ravi[2], Michael Sangid[2]
[1]Sandia National Laboratories, Albuquerque, NM, 87905
[2]Purdue University, West Lafayette, IN, 47907

The role of bulk microstructure on high strain rate behavior is examined through a suite of high energy X-ray characterization techniques, towards illuminating our understanding of material damage. Two materials have been examined – commercially pure Aluminum and 316L stainless steel. The X-ray characterization has been performed at the Cornell high-energy synchrotron source to identify, non-destructively, the 3D bulk microstructure and the grain-level micromechanical fields in each grain within the region of interest. For the Al experiment, a series of samples were characterization, as shown in Fig. A-6(a) prior to the samples being subjected to high strain rate loading (~10^2 1/s) to failure. Future work will use the characterized microstructure to correlate with the porosity on the post mortem fracture surfaces and rationalize the variability in the observed dynamic behavior (Fig. A-6b)) based on crystal plasticity modeling.

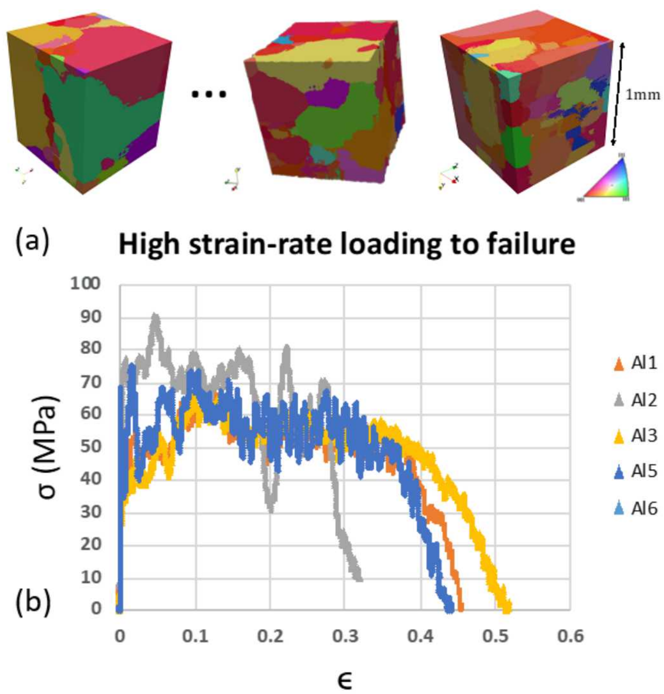

Figure A-6. (a) HEDM grain level stress distribution and (b) stress-strain response via Kolsky bar loading

The stainless steel experiment compares the grain-level stress distribution obtained by continuous quasi-static loading (Fig. A-7(a)) and after interrupted high strain loading (Fig. A-7(b)) with a Kolsky bar. The objective is to identify how the micromechanical fields, including the stress values in individual grains nd their grain interactions, are dictated by their deformation mechanics and strain rate sensitivity of grain averaged stress response. Towards this end, sub-granular misorientation before and after loading will be examined to identify the deformation mechanics and degree of strain localization. The results of this work provide key insights into the high strain rate deformation and damage mechanisms, which can be used in future modeling efforts to predict the dynamic behavior of the material. Delays were experienced in this project due to changing material systems, availability of beamtime necessary for synchrotron-based characterization, and hardware availability to conduct high strain rate loading, but the Purdue team will continue this work towards completion of the overarching goals.

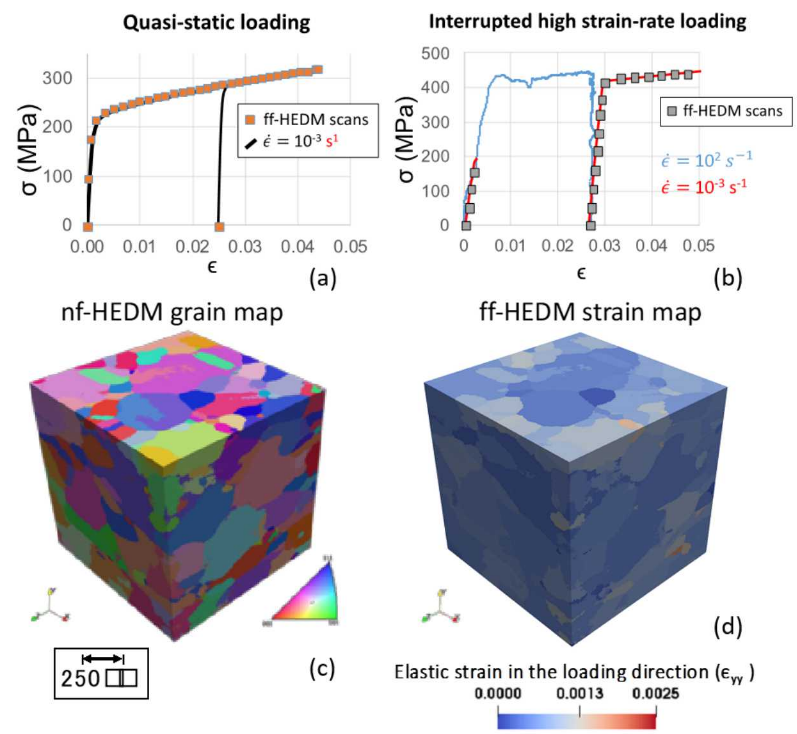

Figure A-7. (a) Quasi-static and (b) dynamic load/unload/reload curves (c) near-field grain map and (d) far field strain map

DISTRIBUTION

Email—Internal

Name	Org.	Sandia Email Address
Technical Library	01177	libref@sandia.gov

This page left blank

This page left blank

Sandia National Laboratories

Sandia National Laboratories is a multimission laboratory managed and operated by National Technology & Engineering Solutions of Sandia LLC, a wholly owned subsidiary of Honeywell International Inc. for the U.S. Department of Energy's National Nuclear Security Administration under contract DE-NA0003525.